International Symposium
On Turbulence and Shear Flow
Phenomena (TSFP-8)
August 28 - 30, 2013 Poitiers, France

DECAY OF THE TURBULENT WAKE FROM THE SUPERSONIC MICRO RAMP

Zhengzhong Sun
Department of Aerospace Engineering
Delft University of Technology
Kluyverweg 2, 2629HT, Delft, the Netherlands
z.sun@tudelft.nl

Ferry F. J. Schrijer
Department of Aerospace Engineering
Delft University of Technology
Kluyverweg 2, 2629HT, Delft, the Netherlands
f.f.j.schrijer@tudelft.nl

Bas W. van Oudheusden
Department of Aerospace Engineering
Delft University of Technology
Kluyverweg 2, 2629HT, Delft, the Netherlands
b.w.vanoudheusden@tudelft.nl

Fulvio Scarano
Department of Aerospace Engineering
Delft University of Technology
Kluyverweg 2, 2629HT, Delft, the Netherlands
f.scarano@tudelft.nl

ABSTRACT

The wake resulting from two micro ramps operating in a supersonic boundary layer at $Ma = 2.0$ is investigated by means of PIV. Two micro ramps are investigated with height of 60% and 80% of the undisturbed boundary layer with thickness of 5.2 mm. The measurement domain encompasses the range from 10 to 32 ramp heights downstream of the device. The decay properties are evaluated in terms of time-averaged and root-mean-square (RMS) statistics. In the time-averaged flow field, the recovery of the imparted momentum deficit and the decay of upwash motion are revealed. The RMS fluctuations of the velocity components exhibit strong anisotropy at upstream locations but develop into a more isotropic regime downstream. The Kelvin-Helmholtz (K-H) instability at the upper shear layer further develops with the onset of vortex pairing. The wavelength evolution is estimated using statistic-based spatial auto-correlation. A marked transition with the wavelength nearly doubled is observed across the pairing regime.

INTRODUCTION

The micro vortex generator (MVG) is gradually receiving research interests in the area of aerospace engineering. Initially proposed for external aerodynamic applications, where it was placed on wing flap to enhance performance at high-lift configurations (Lin (2002)). The MVG is now also considered for internal flow systems, especially for supersonic air intakes, where shock wave boundary layer interaction (SWBLI) is encountered (Babinsky *et al.* (2009)). Flow separation may occur when the shock induced adverse pressure gradient is large enough. The flow separation associated to SWBLI is highly unsteady and introduces in turn undesired spatial and temporal fluctuations in the engine components placed downstream. As a result, one of the primary objectives of MVG has been set to reduce flow separation and to stabilize the interaction region.

A number of baseline experimental studies have been carried out to investigate the effectiveness of MVGs towards SWBLI involving oblique or normal shock waves and positive effects have been received (Holden & Babinsky (2007) Babinsky *et al.* (2009)). Additionally, fundamental studies of the micro ramp flow without the presence of SWBLI have been performed to improve the understanding of the physical mechanisms occurring inside the resulted wake (Nolan & Babinsky (2011)). The momentum deficit and the upwash motion resulted from the vortical motion are revealed as the major flow structures in the mean flow (Babinsky *et al.* (2009) Nolan & Babinsky (2011)). Their decay behavior in the center plane for a longer streamwise distance have not been carefully studied, although Herges *et al.* (2008) studied the wake decay under the effect of normal shock wave boundary layer interaction. The micro ramp wake have been investigated by Babinsky *et al.* (2009), where the velocity profiles at four streamwise positions are measured through LDA. This series of measurements was later taken as the datum for the numerical studies. A Reynolds-averaged Navier-Stokes (RANS) simulation with immersed-boundary treatment was performed by Ghosh *et al.* (2010) ($Ma = 2.5$, $h/\delta = 0.46, 0.92$) and the velocity profiles were compared with the experiment. Interestingly, an acceptable agreement was only achieved for the larger micro-ramp ($h/\delta = 0.92$). As a result, further experimental study of the streamwise decay, particularly in the symmetry plane, is needed not only for the reason of revealing the decay behavior but also for further code validation activities.

Because of the generation of Kelvin-Helmholtz instability taking place at the interface between the wake region and free stream, additional vortices, namely the K-H vortices, are generated in the cross flow plane with intermittency. According to the experimental work of Sun *et al.* (2012), the K-H vortex interacts with the streamwise vortex filaments. Thus the decay of the flow instability becomes critical and needs to be studied. Since the decay of the typical shear layer instability is characterized by vortex pairing, the pairing process becomes another topic when studying the instantaneous snapshots.

With purposes stated above, the current experiments are aimed at the characterization of the far wake (beyond 20

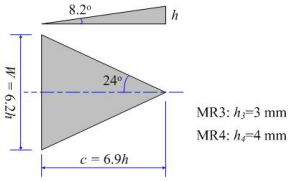

Figure 1. Micro Ramp Models.

ramp heights) and a large measurement domain extending from approximately $12h$ to $32h$ is achieved making use of the planar PIV technique with one large format CCD camera. In the attempt to draw some conclusions on the scaling laws for the wake decay, two values are investigated for the ratio between the micro-ramp height and the boundary layer thickness (h/δ). This is achieved by selecting ramps of 3 mm and 4 mm height.

The following section describes the details of the experiments. In the discussion of results, the decay of the micro ramp wake is elaborated through the time-averaged data and turbulent statistics. The analysis of the instantaneous realizations focuses on the observation of signatures of vortex pairing and proofs are provided through spatial auto-correlation.

EXPERIMENTAL SETUP

Wind Tunnel and Micro Ramps

The experiments were carried out in the supersonic wind tunnel ST-15 in the Delft University of Technology. The wind tunnel was operated at $Ma = 2.0$. The flow in the wind tunnel took about $2s$ to be stable and the duration for each measurement was approximately $70s$ allowing 100 image-pairs to be recorded. The temperature drop within each experiment was about $2°C$, which is considered negligible, thus the velocity can be regarded as constant. The turbulent boundary layer that develops on the bottom wall was used to interact with the micro ramp, and it obtains a thickness of 5.2 mm in the test section. The displacement thickness and the momentum thickness are later determined to be 0.59 mm and 0.48 mm, respectively, resulting in an incompressible shape factor of $H = 1.2$.

The micro ramp geometry follows that suggested in the work of Anderson *et al.* (2006). Two ramps are considered with heights of $h = 3$ and 4 mm, corresponding to 57% and 77% of the undisturbed turbulent boundary layer thickness. These two devices are later referred as **MR3** ($h = 3$ mm) and **MR4** ($h = 4$ mm) in the remainder. The micro ramp chord length is $c = 7.5h$ and the half sweep angle is $\alpha = 24°$, the detailed geometrical dimension of the micro ramp is sketched in figure 1. A single micro ramp was installed along the centerline of the wind tunnel test section. The measurements were taken at the center plane of each micro ramp. The origin of the coordinate system is placed at the junction of the micro-ramp trailing edge and the flow floor with x-axis pointing downstream and y-axis pointing the wall-normal direction. The arrangement of the FOVs and the coordinate system are shown together in figure 2.

PIV Measurement

The laser illumination was provided by a Spectra-Physics Quanta Ray double-pulsed Nd-Yag laser with 400 mJ pulse energy and 6 ns pulse duration at a wavelength of 532 nm. A rigid periscope probe containing a combination

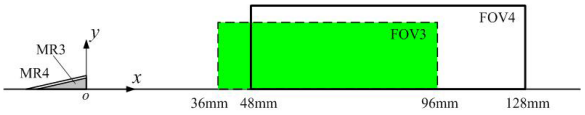

Figure 2. PIV Field of Views.

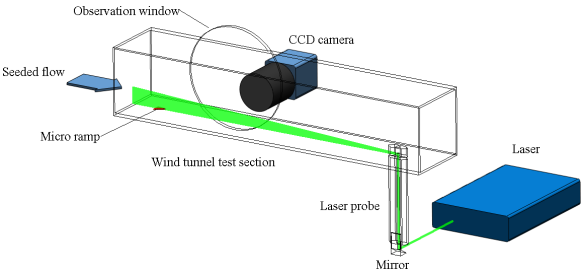

Figure 3. PIV experimental setup.

of optics was used to introduce the laser beam into the test section, and it was vertically installed from the bottom wall downstream the test section. By tuning the focus of the embedded optics inside the probe, the laser beam was formed into a thin sheet with approximately 2 mm thickness for the FOVs.

Di-ethyl-hexyl-sebacate (DEHS) droplet with nominal diameter of approximately $1\mu m$ was used as the seeding particle. A relaxation time of about $2\mu s$ for the DEHS particle was determined by Ragni *et al.* (2011) in a Mach 2.0 flow. The particles were injected into the settling chamber through a seeding probe with multiple orifices. The injection position was carefully chosen on the lower surface inside the settling chamber, thus a locally seeded flow in the turbulent boundary layer was achieved.

The particle images were recorded by one LaVision Imager Pro LX CCD camera (4900×3300 pixels, pixel size $7.5\mu m$, 12 bits). Since the measurement domain was rather elongated along the streamwise direction, the region of interest in the sensor was reduced along the vertical direction with a resulting FOV of $65 \times 18mm^2$ and $82 \times 24mm^2$ for FOV3 and FOV4 respectively. The resulting digital image resolution is 70.42 pixel/mm for FOV3 and 43.08 pixel/mm for FOV4. A total 400 single-exposure double-frame image pairs were recorded at a rate of 1.5 Hz that allow the statistical analysis of the flow field. A Nikon objective of 105 mm focal length was used. The lens aperture was set at $f_\# = 5.6$, which offers a sufficient focal depth also accounting for aero-optical aberration effects. The time interval between pulses was set at $1\mu s$, which allows the displacement of particles in the free stream region was approximately 36 pixels for MR3 and 22 pixels for MR4. Considering a measurement precision of approximately 0.1 pixels, the dynamic velocity range for the two experiments exceeds 300 and 200 for MR3 and MR4 respectively. The experimental setup is schematically drawn in figure 3.

Measurement Uncertainty

In view of the utilization of the present data for future comparison with other numerical simulations or experiments, an upper boundary is given here for the measurement uncertainty. It is considered that the uncertainty originating from PIV measurement dominates the overall experimental errors. The uncertainty due to the flow facility, the temperature effects etc. is deemed to have a minor component.

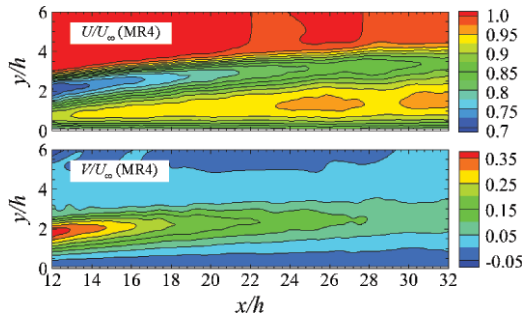

Figure 4. Contours of mean velocity components of MR4: (a) streamwise velocity; (b) wall-normal velocity.

The effects of the finite data ensemble size, the image analysis (cross-correlation) algorithm and finite particle tracers response time are considered here.

Each dataset is composed of 400 uncorrelated realizations. The uncertainty of averaged velocity components is estimated to be $0.8\%U_\infty$ in the wake region where the largest velocity fluctuations occur. Accordingly, the uncertainty of $\langle u' \rangle$ and $\langle u'v' \rangle$ were estimated to be $5\%\langle u' \rangle_{max}$ and $12\%\langle u'v' \rangle_{max}$, respectively. The cross-correlation for planar PIV is conservatively assumed to have an uncertainty of 0.1 pixel, which corresponds to $0.5\%U_\infty$. As a result, the uncertainty of the mean velocity is not affected by the measurement noise.

The measured vector field is given over a regular grid and each vector results from the cross-correlation over the kernel used for spatial cross-correlation. The current window size is about 20% of the wave-length of K-H wave and considering the given spatial response in Schrijer & Scarano (2008) the expected amplitude modulation will not exceed $2\%U_\infty$.

The response time of the DEHS tracer particle should also be considered. According to the experiment of Ragni *et al.* (2011), the response time was estimated to be $1.92\mu s$ for DEHS particle. By multiplying the response time and the relevant particle acceleration, which is estimated to be $5 \times 106 m/s^2$ according to the centrifugal acceleration in the vortical motion, the uncertainty results to be approximately $2\%U_\infty$.

RESULTS AND DISCUSSION

Decay of Mean Flow

The time-averaged velocity field is obtained by ensemble averaging the 400 instantaneous uncorrelated realizations. The streamwise and wall-normal coordinates are expressed in non-dimensional units using the ramp height.

Streamwise velocity Similar flow fields are produced by both micro ramps, thus only the velocity contours of MR4 are shown in figure 4. According to figure 4(a), the wake features a pronounced velocity deficit with a minimum velocity that moves away from the wall nonlinearly when developing downstream. The rate at which the maximum deficit is lifted off the wall decreases downstream as expected by the lower intensity of the upwash motion induced by the primary pair of vortices. A near horizontal wake is thus produced at the end of the domain.

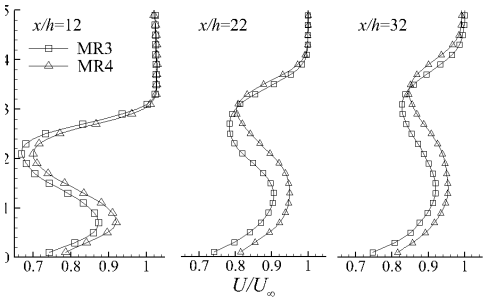

Figure 5. Profiles of mean streamwise velocity.

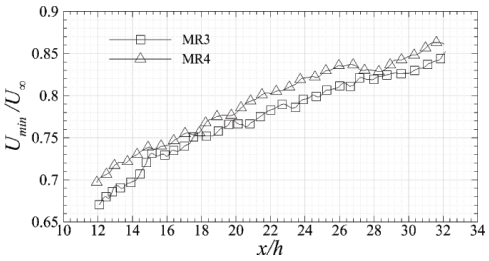

Figure 6. Evolution of maximum deficit velocity.

A detailed analysis of the streamwise velocity evolution can be better revealed by selecting wall-normal profiles at three positions, i.e. $x/h = 12, 22 and 32$, see figure 5. The maximum deficit corresponds to a velocity of approximately 70% of the free-stream value and is located at two ramp heights at $x/h = 12$. It weakens and moves upward due to the strong turbulent mixing occurring at the shear layer. As a result, the dip portion in the profile is enlarged and flattened. Although slight discrepancy of the profiles of MR3 and MR4 can be observed in the deficit region, the chosen scaling offers a better collapse when compared to scaling based on a boundary layer length scale.

Larger difference of velocity magnitude can be observed in the lower neck region, namely the region between the deficit and wall. Since the larger micro ramp (MR4) emerges more above the momentum thickness and the recirculation of high-momentum fluid penetrates deeper at the bottom of the wake, higher magnitude is resulted there. This discrepancy indicates that this part does not follow a scaling with the ramp height.

The wake recovery is addressed following the streamwise evolution of the maximum deficit velocity, see figure 6. Both ramps exhibit a similar recovery rate when expressed in non-dimensional coordinates. The minimum velocity U_{min} of MR4 increases from $0.7U_\infty$ at $x/h = 12$ to $0.86U_\infty$ at $x/h = 32$, while that of MR3 increases from $0.67U_\infty$ to $0.84U_\infty$. In both cases it appears that the recovery occurs at a rate slightly lower than linear. Further normalization with the maximum deficit velocity magnitude at $x/h = 12$ allows both evolution curves to collapse. By performing a regression with exponential function, the decay can be expressed through:

$$\frac{U_{min}}{U_{12}} = -1.5e^{-0.037\frac{x}{h}} \quad (1)$$

where the small exponent of -0.037 conforms to the near-linear recovery and U_{12} is the maximum deficit velocity at $x/h = 12$.

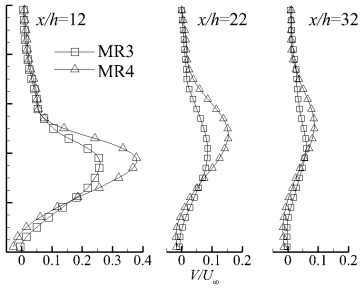

Figure 7. Profiles of wall-normal velocity.

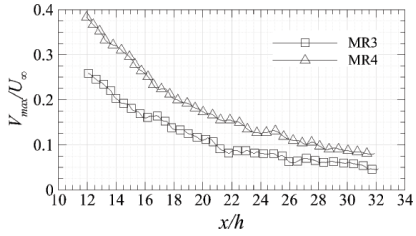

Figure 8. Evolution of maximum upwash velocity.

Wall-normal velocity The time-averaged wall normal velocity is studied in a similar scheme as the streamwise velocity. In the center plane, an upwash region is coalesced from streamwise vortex pair, see the contour of wall-normal velocity of MR4 in figure 4(b). Unlike the velocity deficit, the elevation of upwash is less steep. A much stronger upwash is produced by MR4 and it is associated to the stronger trailing vortex.

The difference of the upwash strength is further addressed through the v-profiles, see figure 7. The significant mismatch of the v-profiles suggests the dependence of upwash intensity on the micro ramp size. At $x/h = 12$, the V_{max} of MR3 is $0.20U_\infty$, which is only 52% of that of MR4. Upwash recovery is obvious through the flattening of profiles, but it is more straightforward in the streamwise evolution of V_{max} in figure 8. The intensity discrepancy becomes smaller instead of being maintained, which could be reasoned as the close strength of streamwise vortices of MR3 and MR4 regardless of their distinct magnitudes at upstream. Similarly, by normalization of the maximum upwash velocity with that at $x/h = 12$ the two curves collapse, and a decay following

$$\frac{V_{max}}{V_{12}} = 2.845e^{-0.09\frac{x}{h}} \qquad (2)$$

is achieved by fit using exponential function, where V_{12} is the maximum upwash at $x/h = 12$. Comparing the current exponent with that of equation1, the maximum upwash decays 2.4 times faster. It is well understood that the velocity deficit is a product of vortical activity, the deficit center is presumably to be closely associated with the peak upwash, where the maximum momentum exchange is executed. In order to detect the relevance of the two significant flow structures, the trajectories of U_{min} and V_{max} are compared, see figure 12. The U_{min} is observed to be produced higher instead of overlapping with V_{max}. The vertical offset suggests that the deficit center is not produced as soon as the peak upwash is reached, but is delayed. This offset distance grows following the development of the wake, it thus

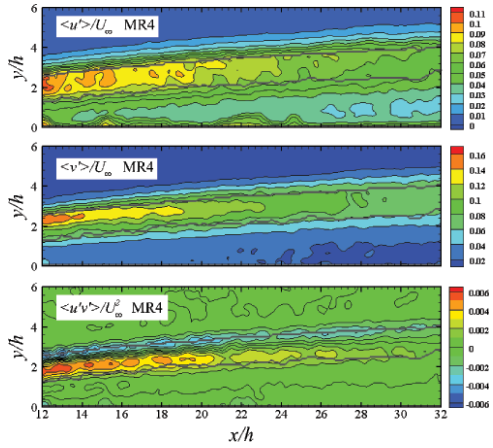

Figure 9. Contour of turbulent quantities.

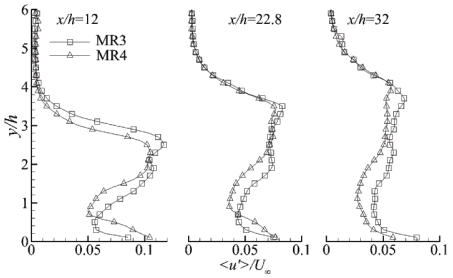

Figure 10. Profile of $\langle u' \rangle$ at $x/h = 12, 22.8, 32$.

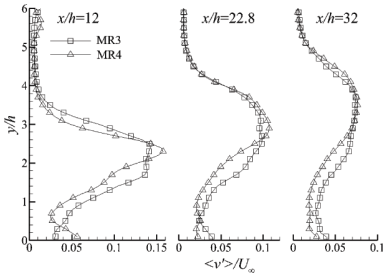

Figure 11. Profile of $\langle v' \rangle$ at $x/h = 12, 22.8, 32$.

confirms the weaker vortices downstream which are less effective in lifting the wake.

DECAY OF TURBULENT PROPERTY

The decay of turbulent property is investigated through the root-mean-square (RMS) of velocity components ($\langle u' \rangle$ and $\langle v' \rangle$) and the Reynolds shear stress ($\overline{u'v'}$).

Velocity Fluctuations

Increased level of velocity fluctuations occurs in the micro ramp wake, an overall observation can be achieved in the contours of $\langle u' \rangle$ and $\langle v' \rangle$ in figure 9(a)(b), respectively. Note that the upper and lower edges of the wake defined by the inflection points in the velocity profiles are overlaid for reference. The velocity fluctuations follow the trend of the wake elevation, and the decay of fluctuation magnitude is evident from upstream to downstream. For example, $\langle u' \rangle_{MR4}$ is $0.06U_\infty$ at $x/h = 32$ which is about 60% of the magnitude at $x/h = 12$. The increased fluctuation within the wake was also measured by Herges *et al.* (2008) using

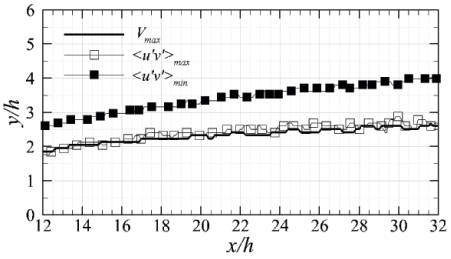

Figure 12. Trajectories of peak activities of MR4.

PIV and it was explained as a consequence of the streamwise vortices. However, current visualization reveals that peaks of $\langle u' \rangle$ and $\langle v' \rangle$ concentrate closer to the upper edge, where the K-H phenomenon dominates, and the enhanced fluctuation is more likely to associate with the flow instability, which is able to undulate the flow through the embedded K-H vortices.

More insights can be achieved from the profiles of $\langle u' \rangle$ and $\langle v' \rangle$. According to the profiles of $\langle u' \rangle$ and $\langle v' \rangle$ at $x/h = 12, 22.8$ and 32 in figure 10, the wake fluctuation is represented by the elevated portion within the profiles. Dual peaks are especially clear in $\langle u' \rangle$ and $\langle v' \rangle$ profiles of MR3 at $x/h = 12$ and 22.8 with one close to the upper edge and the other in the lower edge. The upper peak confirms the earlier observation in the contours, while the lower peak indicates the flow instability at the lower edge, which will be discussed in the section of instantaneous flow. In the profiles at $x/h = 32$, the hump-like peaks become a plateau, which means that the flow instability at both ends already decrease to a weaker strength at that point. The reason why the hump-like peaks are not obvious in the profiles of MR4 could be the relatively low seeding density in the positions of K-H vortices, which is stronger than that produced by MR3 and subsequently produce larger centrifugal forces. Vectors in those regions were therefore interpolated by the surrounding areas, showing similar degree of fluctuation. Further comparison between $\langle u' \rangle$ and $\langle v' \rangle$ finds that at upstream $\langle v' \rangle_{max}$ is approximately 1.6 times of $\langle u' \rangle_{max}$ at $x/h = 12$, suggesting strong anisotropy upstream. But similar peak magnitudes, approximately $0.06U_\infty$, are achieved at $x/h = 32$, which means the wake tends to behave as isotropic turbulence in the late flow due to the wake decay.

Reynolds Shear Stress

The Reynolds shear stress ($\overline{u'v'}$) is a measure of the shear strength in the flow. Concentration of negative peaks are thus produced along the upper edge, see figure 9(c). Symmetric peaks of positive value can also be observed. They are above the lower edge in the first half of current FOV, and start to fall over the lower edge in the next half. Comparison of the trajectories of quantities including $\overline{u'v'}_{max}$, $\overline{u'v'}_{min}$ and V_{max} gives the relations among them. The three trajectories of MR4 are shown in figure 12. It is evident that $\overline{u'v'}_{max}$ follows V_{max}. As a result, the positive peaks of $\overline{u'v'}$ is more likely to associate with the event of peak upwash instead of the shear activity at the lower edge.

INSTANTANEOUS FLOW: VORTEX PAIRING

The instantaneous flow behaves distinctively from the mean flow and is featured by the Kelvin-Helmholtz (K-H) instability, see one flow realization of MR4 in figure 13. The K-H instability is characterized by the sinusoidal-like wave

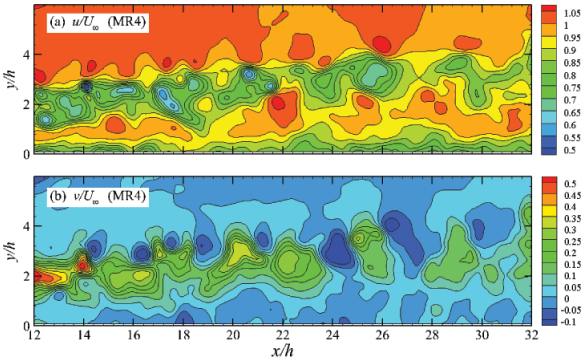

Figure 13. Contour of one instantaneous velocity field of MR4: (a)streanwise component, (b)wall-normal component.

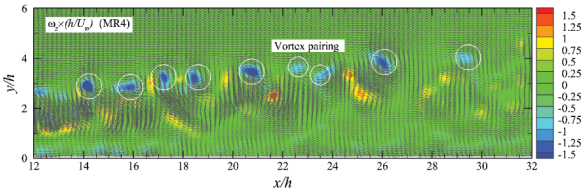

Figure 14. Contour of instantaneous vorticity field.

at the top of the wake, and a train of vortex is shed following the development of unstable wave. The swirling vectors of the K-H vortices in figure 14 are visualized by subtracting a constant value of $0.87U_\infty$ from the streamwise vector component. The vortex shedding is a common phenomenon existing in the wake of a bluff body, and a large body of studies has been devoted into this phenomenon. However in the micro ramp flow, this phenomenon has not received adequate attention until the studies of Li & Liu (2010) and Sun *et al.* (2012). One immediate result from the vortical activity is the disruption of the velocity field, which consequently results in local high speed and low speed packets on either side of the K-H wave. The relatively long streamwise extent of current study allows the study of vortex paring which is a typical vortical activity occurs in the process of vortex shedding caused by flow instability.

Vortex pairing is featured with a pair of closing-up vortices in the process of vortex shedding and subsequently results in a larger wavelength downstream after the merge of the previous two. One pair of vortices which are about to merge can be seen at around $x/h = 23$ in figure 14, and the two pairing vortices have a distance of about $1h$.

In order to identify the onset of vortex pairing and the evolution of wave-length, auto-correlation of the instantaneous vorticity field is adopted. The procedure of auto-correlation is the same as that used in Sun *et al.* (2012). For the current purpose, the auto-correlation window is shifted towards various streamwise positions. Different auto-correlation window sizes are also used to exclude the error associated with window size (WS).

The wave-length evolution of MR4 retrieved using four WSs, namely $WS = 5 \sim 8h$, are presented in figure 15(a). Similar evolution trend is returned by most window sizes, although there is some scattering. A critical result is given by $WS = 5h$, as it underestimates the wavelength at several positions, especially in the region $x/h = 20 \sim 22$. Further averaging of the wave-length evolution retrieved from the valid WSs provides a smoothed result, see figure 15(b).

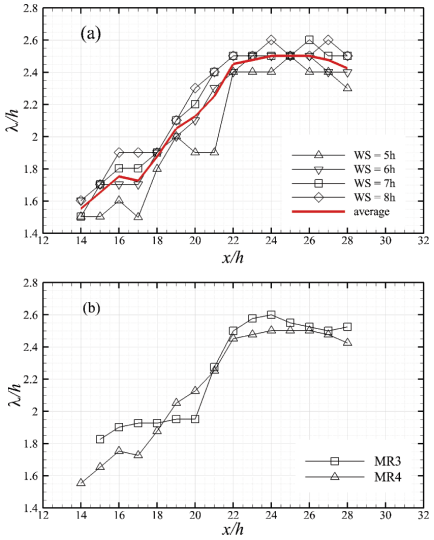

Figure 15. Evolution of wave-length: (a)window size effect for MR4; (b)averaged evolution.

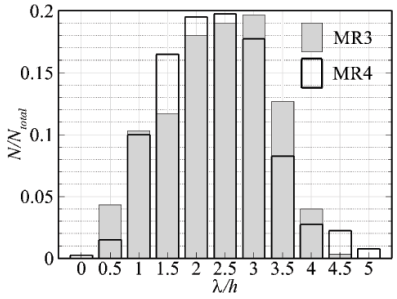

Figure 16. Wave-length distribution in $x/h = 25 \sim 32$.

The wave-length is approximately $1.8h$ and $1.6h$ for MR3 and MR4 respectively at upstream. An evident jump occurs at around $x/h = 20$ and increases the wave-length to about $2.5h$ till the end. In the ideal condition, the pairing is expected to result in a doubled wave-length, which is however less than doubled in the current result. This can be ascribed to the averaging effects of both the paired and unpaired cases in the downstream regions. A histogram of wave-length in the region of $x/h = 25 \sim 32$, see figure 16, is then used to reveal the occurrence of vortex pairing. Doubled wave-length, approximately in the range of $\lambda = 3 \sim 4h$, is essentially produced and it accounts for about 37% and 30% of the entrie ensemble for MR3 and MR4 respectively, suggesting that vortex pairing is slightly less dominant within current measurements.

Conclusions

Based on the above discussions of the time-averaged velocity, the turbulent statistics and the statistical analysis of the instantaneous flow fields, the properties of the micro ramp wake decay at the center plane and the associated vortical activity could be concluded.

Similar magnitude of streamwise velocity deficit is produced by the interested micro ramps, whereas a stronger upwash is generated by MR4, which is ascribed to the stronger streamwise vortices resulted from that device. The regions containing velocity deficit and the upwash have the major extension in streamwise direction, but exhibit different rates of decay. Comparing the trajectories of maximum deficit and peak upwash, the former is produced higher suggesting that there is delayed effect in generating the velocity deficit.

Anisotropy of velocity fluctuation is present in the micro ramp wake at upstream with $\langle v' \rangle$ stronger than $\langle u' \rangle$, whereas both quantities obtain similar intensity at downstream due to the faster decay of $\langle v' \rangle$. The Reynolds shear stress $\overline{u'v'}$ obtains near-symmetric peaks at the center plane. The negative peak is associated to the vortex production and follows the position of upper shear layer, while the positive peak is likely to be associate to upwash activity as trajectories of $\overline{u'v'}_{max}$ and V_{max} overlap.

In the instantaneous flow, the well-organized time-averaged flow is greatly altered by the K-H instability and the vortical flow obtains great complexity. Observation of the instantaneous realizations as well as the wave-length evolution retrieved from statistical spatial auto-correlation confirm the vortex pairing, which determines the transition of micro ramp wake.

REFERENCES

Anderson, B. H., H., Tinapple & Surber, L. 2006 Optimal control of shock wave turbulent boundary layer interactions using micro-array actuation. *AIAA paper 2006-3197* .

Babinsky, H., Li, Y. & PittFord, C. W. 2009 Microramp control of supersonic oblique shcok-wave/boundary-layer interactions. *AIAA J.* **47**, 668–675.

Ghosh, S., Choi, J-I & Edwards, J. 2010 Numerical simulations of effects of micro vortex generators using immersed-boundary methods. *AIAA J.* **48**, 92–103.

Herges, T., Kroeker, E., Elliott, G. & Dutton, C. 2008 Microramp flow control of normal shock/boundary-layer interactions. *AIAA J.* **48**, 2529–2542.

Holden, H. & Babinsky, H. 2007 Effects of microvortex generators on the separated normal shock/boundary layer interactions. *J. Aircraft* **44**, 170–174.

Li, Q. & Liu, C. 2010 Les for supersonic ramp control flow using mvg at $m = 2.5$ and re_θ=1440. *AIAA paper 2010-592* .

Lin, J. C. 2002 Review of research on low-profile vortex generators to control boundary-layer separation. *Progress in Aerospace Sciences* **38**, 389–420.

Lu, F. K., Pierce, A. & Shih, Y. 2010 Experimental study of the near wake of micro vortex generators in supersonic flow. *AIAA paper 2010-4623* .

Nolan, W. R. & Babinsky, H. 2011 Characterization of mico-vortex generators in supersonic flows. *AIAA paper 2011-71* .

Ragni, D., Schrijer, F.F.J., van Oudheusden, B. W. & Scarano, F. 2011 Particle tracer response across shocks measured by piv. *Exp. Fluids* **50**, 53–64.

Schrijer, F.F.J. & Scarano, F. 2008 Effect of predictor-corrector filtering on the stability and spatial resolution of iterative piv interrogation. *Exp. Fluids* **45**, 927–941.

Sun, Z., Schrijer, F.F.J., Scarano, F. & van Oudheusden, B. W. 2012 The three-dimensional flow organization past a micro-ramp in a supersonic boundary layer. *Physics Fluids* **24**, 055105–22.